International Journal of Multiphase Flow 34 (2008) 1108–1118

Contents lists available at ScienceDirect

International Journal of Multiphase Flow

journal homepage: www.elsevier.com/locate/ijmulflow

Segmented gas–liquid flow characterization in rectangular microchannels

Donata M. Fries [1], Franz Trachsel [1], Philipp Rudolf von Rohr *

Institute of Process Engineering, ETH Zurich, Sonneggstrasse 3, 8092 Zurich, Switzerland

ARTICLE INFO

Article history:
Received 3 September 2007
Received in revised form 30 April 2008
Accepted 15 July 2008
Available online 26 July 2008

Keywords:
Taylor flow
Optical characterization
Film thickness
Pressure drop
Phase distribution

ABSTRACT

We used optical methods such as Laser Induced Fluorescence (LIF) and confocal Laser Scanning Microscopy (LSM) to characterize gas–liquid phase distribution in rectangular microchannels. Using a 2 m long microchannel with a hydraulic diameter of 200 μm enables the precise measurement of important parameters such as liquid slug length, bubble length, pressure drop and film thickness at the wall as well as in the corner of the microchannel for low Capillary numbers (*Ca*) ranging from 2×10^{-4} to 1×10^{-2}. This range of *Ca* was obtained by using different fluid pairs such as ethanol, water and different concentrated aqueous solutions of glycerol in combination with nitrogen.

The investigated segmented gas–liquid flow (Taylor flow) was very stable, meaning a standard deviation of the measured gas bubble lengths of below 5% and 10% for the liquid slug length, respectively. Using higher viscosities than 10 mPas resulted in an unstable flow – mainly due to the pressure drop. For viscosities in the range of 10 mPas the flow pattern changes: the slug lengths are much longer than the channel diameter.

We demonstrate that the film thickness in the corner slightly decreases with *Ca*. For low *Ca* the film thickness at the wall stayed nearly constant. We observe a contribution of the film in the corner to the total film area of about 70%. The obtained gas bubble length depends mainly on the viscosity and on the pressure at the gas inlet. As the measured liquid holdup is in all cases higher than the theoretical holdup defined by the flow rates, the bubbles move faster than the liquid phase. The measured values are compared with literature data.

1. Introduction

Microreaction technologies are of great interest for industry and research in chemical engineering. The excellent heat and mass transfer properties, continuous operation mode, advanced reaction control and enhanced process safety enable microreactors as an efficient tool for the fine chemical industry and provide new possibilities in the performance of hazardous reactions (Jensen, 2001). Depending on the microfluidic channel geometry and the flow rates, three main flow regimes for gas liquid co-current flow in microchannels can be differentiated: (1) The bubble flow regime, where sphere-like gas bubbles flow within the continuous liquid phase. (2) Taylor flow, which is discussed in this study, is characterized by gas bubbles (gas bubble length l_B < channel diameter d_h) alternating with short (liquid slug length $l_S \sim d_h$) liquid slugs. (3) Annular flow is defined as a continuous gas core surrounded by a liquid film at the channel wall. The liquid film in a rectangular microchannel consists of a thin liquid layer at the channel wall and liquid filled channel corners.

Taylor flow in microreactors has attracted great interest for many chemical applications (e.g., Khan et al., 2004). By a recirculating motion in the liquid slugs mass transfer is enhanced between the gaseous and the liquid phase and between the bulk liquid and the liquid film (Waelchli and Rudolf von Rohr, 2006). Compared to single phase flow, Taylor flow reduces axial dispersion (Trachsel et al., 2005). In addition to recirculation, the bubble length, slug length, film thickness and their distributions are other important parameters for an optimized mass transfer. Knowledge about bubble length, slug length and film thickness is crucial for a quantitative analysis of the axial dispersion, gas–liquid mass transfer coefficient and the transport to a catalytic channel wall through the liquid film. Taylor flow in circular and rectangular capillaries was reviewed by Kreutzer et al. (2005a).

1.1. Pressure drop

The total pressure drop in gas–liquid flow consists of the pressure drop caused by the friction, pressure drop due to acceleration, caused by gravity and by the shape of the bubbles.

$$(\Delta p)_{\text{tot}} = (\Delta p)_{\text{fric}} + (\Delta p)_{\text{acc}} + (\Delta p)_{\text{grav}} + (\Delta p)_{\text{B}} \quad (1)$$

It can be assumed, that the pressure drop due to friction is the dominant part. The pressure drop caused by acceleration can be

---

* Corresponding author. Tel.: +41 44 632 43 17; fax: +41 44 632 13 25.
E-mail address: vonrohr@ipe.mavt.ethz.ch (P. Rudolf von Rohr).

[1] These authors contributed equally to this article and are listed in alphabetical order.

0301-9322/$ - see front matter © 2008 Elsevier Ltd. All rights reserved.
doi:10.1016/j.ijmultiphaseflow.2008.07.002

neglected for small pressure drop values. Friedel (1978) stated, that this is the case for $\frac{\Delta p}{p} < 0.2$. Otherwise the increase in the gas holdup and therefore in the volumetric flow rate due to the pressure drop will lead to an increase in the velocities. In this case the pressure drop due to acceleration has to be calculated by:

$$\Delta p_{\mathrm{acc}} = \dot{m}^2 \left(\left[\frac{\dot{x}_G^2}{\rho_G \epsilon_G} + \frac{\dot{x}_{\mathrm{L}}^2}{\rho_{\mathrm{L}} \epsilon_{\mathrm{L}}} \right]_{L=L_{\mathrm{R}}} - \left[\frac{\dot{x}_G^2}{\rho_G \epsilon_G} + \frac{\dot{x}_{\mathrm{L}}^2}{\rho_{\mathrm{L}} \epsilon_{\mathrm{L}}} \right]_{L=0} \right) \tag{2}$$

Δp_{acc} is the pressure drop due to acceleration, $\dot{m}$ is the mass flux, L_{R} is the reactor length, ϵ is the holdup, ρ the density and $\dot{x}$ stands for the mass transport fraction. The subscript G characterizes the gas phase, L denotes the liquid phase. The pressure drop due to gravity, $(\frac{\Delta p}{\Delta L})_{\mathrm{Grav}}$, defined by

$$\left(\frac{\Delta p}{\Delta L} \right)_{\mathrm{Grav}} = (\epsilon_G \rho_G + \epsilon_{\mathrm{L}} \rho_{\mathrm{L}}) g \sin \varphi \tag{3}$$

can be neglected in horizontal pipes, as the inclination angle φ will be 0.

The pressure drop over a moving bubble due to the different shape of the bubble front and bubble tail, caused by surface tension effects, was found by Bretherton (1961) to be

$$\Delta p_{\mathrm{B}} = 3.58 \frac{\sigma}{r} \sqrt[3]{9 Ca^2} \tag{4}$$

r is the bubble radius and Ca is the Capillary number defined as

$$Ca = \frac{\eta u_{\mathrm{B}}}{\sigma}. \tag{5}$$

η is the fluids dynamic viscosity, u_{B} the bubble velocity and σ the surface tension. For Ca calculation, the total superficial velocity was used. The model was validated experimentally in a circular glass tube with a length of 1 m and an inner diameter of $d_{\mathrm{h}} = 1$ mm.

The frictional pressure drop can be calculated by:

$$\left(\frac{\Delta p}{L_{\mathrm{R}}} \right)_{\mathrm{fric}} = f \rho_{\mathrm{L}} j^2 \frac{2}{d_{\mathrm{h}}} \epsilon_{\mathrm{L}} \tag{6}$$

For one-phase flow, the holdup ϵ_{L} is equal to 1. In case of two-phase flow, the velocity j is the sum of the superficial velocity of both phases. For the friction factor f different correlations for Taylor flow can be found in literature. They are summarized in Table 1. In these correlations, l_{S} denotes the liquid slug length whereas the Reynolds number Re is defined as $Re = \rho_{\mathrm{L}} \cdot (j_{\mathrm{L}} + j_{\mathrm{G}}) \cdot d_{\mathrm{h}} / \eta_{\mathrm{L}}$. Since the liquid phase is the continuous one, the liquid fluid properties as well as the velocity of the slug has to be used.

In all these experiments, the observed bubble velocity was slightly increased compared to the superficial velocity, indicating a liquid film surrounding the gas bubble.

Table 1
Correlations for the friction factor f

Reference	Correlation	
Standard, one phase laminar flow	$f = \frac{16}{Re}$	(7)
Bretherton (1961), analytical solution	$f = \frac{16}{Re} \left[1 + 0.465 \frac{d_{\mathrm{h}}}{l_S} \left(\frac{1}{Ca} \right)^{0.33} \right]$	(8)
Kreutzer et al. (2005b), numerical, validated with experiments in a circular capillary for $Re < 50$, $d_{\mathrm{h}} = 2.3$ mm	$f = \frac{16}{Re} \left[1 + 0.17 \frac{d_{\mathrm{h}}}{l_S} \left(\frac{Re}{Ca} \right)^{0.33} \right]$	(9)

Lockhart and Martinelli (1949) proposed, that the pressure drop of two phase flow will be correlated to the equivalent pressure drop in one phase flow by the two-phase multiplier Ψ^2:

$$\left(\frac{\Delta p}{L} \right)_{2P,\mathrm{fric}} = \Psi_{\mathrm{L}}^2 \left(\frac{\Delta p}{L} \right)_{\mathrm{L,fric}} = \Psi_G^2 \left(\frac{\Delta p}{L} \right)_{\mathrm{G,fric}}. \tag{10}$$

Chisholm (1967) stated the dependence of Ψ^2 from the so called Lockhart–Martinelli parameter X and a factor C:

$$X = \sqrt{\frac{(\Delta p / L)_{\mathrm{L}}}{(\Delta p / L)_G}} \tag{11}$$

$$\Psi_{\mathrm{L}}^2 = 1 + \frac{C}{X} + \frac{1}{X^2}, \Psi_G^2 = 1 + CX + X^2. \tag{12}$$

In the past, various correlations for the factor C were proposed. They are summarized in Table 2.

1.2. Phase distribution

The phase distribution can be quantified in different ways: one is the liquid holdup, defined by

$$\epsilon_{\mathrm{L}} = \frac{V_S}{V_S + V_{\mathrm{B}}}. \tag{16}$$

V_{S} and V_{B} stand for the volume of the slug and the bubble, respectively, in a unit cell. Due to the fact that we analyze the length of the gas bubble and liquid slug in the channel center via LIF, the volume of the gas and the liquid phase has to be estimated by assuming the gas bubble front and tail to be a rotational ellipsoid. In contrast to the liquid holdup (Eq. (16)) a volumetric flow ratio can be defined by:

$$\epsilon_{\mathrm{L}}^* = \frac{j_{\mathrm{L}}}{j_{\mathrm{L}} + j_{\mathrm{G}}} \tag{17}$$

These values characterize the relative amount of liquid in the channel.

Additional, the ratio and the sum of the gas bubbles and the liquid slugs can be used to characterize the flow.

1.3. Film thickness

Knowledge about the liquid film thickness is essential, for axial and radial mass transfer analysis. Quantification of axial mass transfer behavior the liquid films in the corner of a rectangular microchannel is of great importance, since the communication of subsequent liquid slugs mainly occurs through the liquid filled corners. Fairbrother and Stubbs (1935) investigated the thickness of the remaining liquid film when a long gas bubble ($l_{\mathrm{B}} > 1.5 d_{\mathrm{h}}$) passes a capillary. Using a 1 m long circular capillary with an inner diameter of $d_{\mathrm{h}} = 2.25$ mm, they found out, that the bubble moves faster than the liquid. Both, the velocity of the bubble and the remaining film thickness were found to be dependent on $\sqrt{Ca}$. The film thickness δ was expressed by

$$\delta = \frac{d_{\mathrm{h}}}{4} \sqrt{Ca}. \tag{18}$$

Table 2
Correlations for the Lockhart–Martinelli factor C

Reference	Correlation	
Chisholm (1967), both phases laminar, circular tube, $d_{\mathrm{h}} = 0.001$–0.025 m	$C = 5$	(13)
Mishima (1996), circular tube, $d_{\mathrm{h}} = 1$–4 mm	$C = 21 \left[1 - e^{(-0.349 d_{\mathrm{h}})} \right]$	(14)
Lee and Lee (2001)	$C = A \cdot \frac{\eta_{\mathrm{L}}^2}{\rho_{\mathrm{L}} \sigma d_{\mathrm{h}}}^{q} Ca^r Re_{Lo}^s$	(15)

Marchessault and Mason (1960) corrected this correlation to

$$\delta = 0.5 d_{\mathrm{h}} \sqrt{\frac{\eta}{\sigma}}\left(-0.05 + 0.89\sqrt{u_{\mathrm{B}}}\right). \tag{19}$$

Taylor (1961) extended the range of experimental data up to $Ca = 2$, where a limiting value of $4\delta/d_{\mathrm{h}} = 0.56$ was suggested. Numerical considerations done by Bretherton (1961), assuming negligible inertia and gravity effects in horizontal capillaries, refined the results done by Fairbrother and Stubbs (1935):

$$\delta = 0.66 d_{\mathrm{h}} Ca^{2/3}. \tag{20}$$

Irandoust and Andersson (1989) did experimental research on upward and downward Taylor flow in vertical tubes of an inner diameter of $d_{\mathrm{h}} = 1$–2 mm and a length of $L = 0.4$ m. They modified the correlation in Eq. (20) to

$$\delta = 0.18 d_{\mathrm{h}}[1 - \exp(-3.1 Ca^{0.54})]. \tag{21}$$

Investigations with varying fluids and varying tube radii done by Aussillous and Quere (2000) gave the following inertia-dependent correlation:

$$\delta \sim d_{\mathrm{h}} \frac{Ca^{2/3}}{1 + Ca^{2/3} - We} \tag{22}$$

with $We = \rho_{\mathrm{L}} u^2/\sigma$. All correlations presented above for liquid film thickness discuss semi-infinite bubbles in circular capillaries. In rectangular microchannel one observes the forming of two different film regions. Fig. 1(a) shows a schematic phase distribution in Taylor flow in capillaries. In contrast to circular capillaries, where a constant film thickness is created (Fig. 1(b)), square capillaries form a corner film region and a wall film region with dimensions of different magnitude (Fig. 1(c)). The gas bubble is non axisymmetric. For the wall film thickness in square capillaries often correlations for circular capillaries were used. The wall film is present only in the middle of the channel. A transition region between the corner and wall film is observed, where the liquid film reaches a minimum thickness. These contact lines of the gas bubble with the channel wall were also discussed by Wong et al. (1995). For higher Ca numbers an axisymmetric gas bubble is formed as the film increases in thickness (Fig. 1(d)). In our observed Taylor flow regime short gas bubbles in the order of several channel diameter occur. Measurements of the liquid film in square capillaries were conducted by Kolb and Cerro (1991) and Thulasidas et al. (1995). The numerical simulation by Hazel and Heil (2002) for the wall film thickness could not be validated by the results from (Kolb and Cerro, 1991). At the limit $Ca \to 0$, (Wong et al., 1995) found the film in rectangular microchannels to be non uniform in thickness in lateral and axial direction.

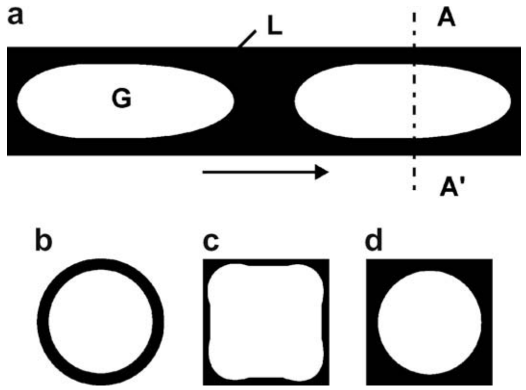

Fig. 1. Scheme of the liquid film distribution in Taylor flow in microchannels. (a) Schematic phase distribution in Taylor flow. The arrow indicates the flow direction. (b) Section A–A' for circular capillaries. (c) Section A–A' at low $Ca(\mathrm{O}(10^{-3}))$. (d) Section A–A' at high $Ca(\mathrm{O}(10^{-1}))$.

In our study we characterize Taylor flow in rectangular microchannels with a hydraulic diameter of ($d_{\mathrm{h}} = 200\ \mu\mathrm{m}$) made of Silicon and glass. Confocal Laser Scanning Microscopy (LSM) and Laser Induced Fluorescence (LIF) are used for the optical investigation of Taylor flow at different liquid and gas flow rates. Bubble and slug lengths as well as their distributions and film thicknesses at the wall and in the corners of the channel were measured. LSM enables a precise spatial measurement of time averaged liquid and gas distribution in a microfluidic channel. Liquid holdup was analyzed by LIF. Measurements were conducted at low Ca in the range of $\mathrm{O}(10^{-4})$–$\mathrm{O}(10^{-2})$. At these low Ca surface tension dominates and little impurities may cause large deviation in film and bubble geometry in the microchannel due to Maragoni effects. Experimental determination of film thickness is crucial since numerical methods have difficulties to resolve the thin films which rearrange over a long axial length scale (Hazel and Heil, 2002; Taha and Cui, 2006).

2. Experimental setup

The microfluidic channel device consists of a 2 m long single channel made of Silicon and glass. The surface roughness of the dry etched channels was 0.15 ± 0.02 μm. A scheme of the microreactor is shown in Fig. 2.

The microreactor was designed to guarantee a continuous and stable gas injection and an enhanced stable two-phase flow, Kreutzer et al. (2006). The gas inlet (Fig. 2, detail A) with a channel width of 100 μm allows a continuous and stable injection of the gas in the liquid stream and a uniform formation of the segmented gas–liquid flow. A scheme of the gas inlet is illustrated in Fig. 2, detail B. Before the gas enters the main channel via a T-junction an inlet zone of meandering channels increases the pressure drop and creates a stable gas injection. The microfluidic channel has a length of $L_{\mathrm{R}} = 2$ m and a height equal to the width of 200 ± 2 μm. Due to the fabrication process the height is constant over the complete chip. The curve radius is large enough to fulfill the assumption of a straight channel. The Dean Number ($Dn = Re\sqrt{d_{\mathrm{h}}/R} = 3 \ldots 70$, R is the radius of the curve) is small enough to prevent recirculation in the liquid slug due to centrifugal forces. The outlet equipped with a gas–liquid separator (Guenther et al., 2005) reduces the pressure fluctuations compared to a common outlet of the gas and liquid phase by a factor of 10. The separator consists of 30 capillaries with a width of 20 μm orthogonal to the main channel.

Flow rates are in the range of 20–60 μL/min for the liquid phase and 30–100 μL/min for the gas phase, relevant for reactions with residence times in the order of minutes. The corresponding superficial velocities are $j_{\mathrm{L}} = 0.008\ \mathrm{m/s} - 0.025\ \mathrm{m/s}$ and $j_{\mathrm{G}} = 0.013\ \mathrm{m/s} - 0.042\ \mathrm{m/s}$. As fluids, ethanol, water and glycerol in aqueous solution at different concentrations and nitrogen were used. The liquid phase was colored with Rhodamine B in a concentration of 5×10^{-5} M and Fluorescein. The physical properties of the used fluids are summarized in Table 3.

The liquid phase was fed with a syringe pump (Harvard Aparatus, accuracy within 0.35% and reproducibility within 0.05%). The gas phase was controlled by a mass flow controller (Bronkhorst, accuracy ±0.5% of reading plus 0.1% full scale). Pressure transducers (Endress and Hauser) with an accuracy of 0.5% full scale were attached to the microreactor 5 cm above the inlet.

3. Measurement methods

3.1. Laser induced fluorescence

The Laser Induced Fluorescence (LIF) measurements were performed on an inverted microscope (Zeiss). This method is widely used for flow characterization in microfluidics, see (Guenther

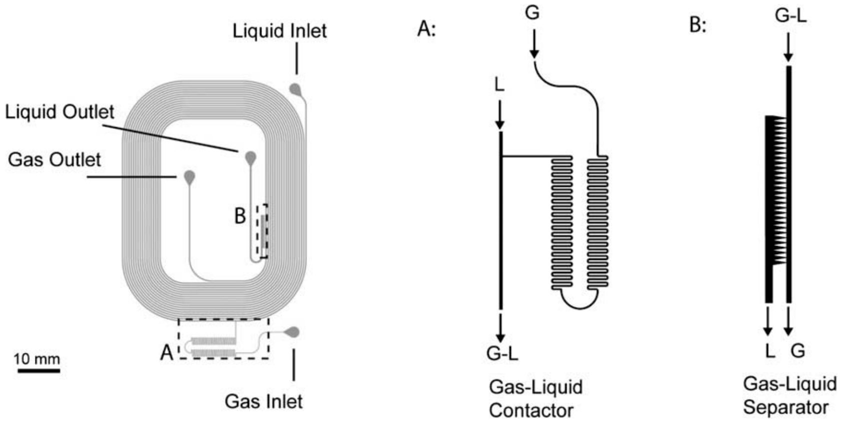

Fig. 2. Scheme of the used reactor, whereas the gas–liquid contactor and the separator provide a stable two-phase flow.

et al., 2005; de Mas et al., 2003; Trachsel et al., 2005; Waelchli and Rudolf von Rohr, 2006). As light source a double-pulsed Nd:YAG-Laser (NewWave) with an illumination time of 5 ns per shot and a minimum time delay of 4 μs between both shots was used. The laser light with a wavelength of 532 nm is absorbed by the Rhodamine B colored liquid phase and orange light is emitted. After passing a dichroic mirror, the emitted light was detected by a CCD camera. The maximum acquisition frequency is 5 Hz for the double-framed double exposed pictures. The system was synchronized by a programmable timing unit (PTU 9, LaVision). Each measurement consists of 200 double-framed double-exposed pictures and was repeated at least one time. The field of view was 1400 μm × 1050 μm. Background uncertainties and light scattering at the channel walls were eliminated by the calibration. The time delay for both exposures was varied between 200 μs and 1000 μs. Before each measurement, the flow was stabilized at least for 30 min.

To determine the velocity of the two phase flow, a high speed camera (LaVision) instead of the CCD camera was used. We took a sequence of 1000 images, recorded with the frequency of 3000 Hz at the gas inlet and analyzed the frequency of the gas bubbles via Fast Fourier transformation using Matlab software. The frequency was used to calculate the bubble velocity.

3.2. Confocal laser scanning microscopy

To increase the depth resolution a confocal Laser Scanning Microscope (LSM 5 Pascal, Zeiss) was used to measure liquid film thickness. The main difference between LSM and conventional microscopy is the pixel-wise (serial) transformation of the object with a pointscanner in LSM, while the object is simultaneously (parallel) transformed in conventional microscopy. The key advantage of LSM is a confocal aperture, which enhances the contrast and reduces scattered light from out of focus object slices. The experimental setup is shown in Fig. 3.

The possibility of depth-wise optical slicing of an object makes this measurement technique beneficial for 3D flow visualization in microchannels by fluorescent microscopy. Depth discrimination and stray light suppression are the main features of confocal LSM. Until now the LSM suffered from its low temporal resolution in the range of 2–3 optical slices per second. Recently high speed confocal scanner, able to acquire 2000 frames per second, were introduced in confocal microscopy for μ-Particle Image Velocimetry (μ-PIV) measurements (Kinoshita et al., 2007). Confocal microscopy was used in microfluidic research mainly for the characterization of mixing (Stroock et al., 2002), 2D and 3D velocity measurements by μ-PIV (Park et al., 2006) and the monitoring of chemical reactions by Raman spectroscopy (Fletcher et al., 2003).

3.2.1. Resolution LSM

In order to represent the resolution independent of the objective used it is necessary to define a new optical coordinate "Airy Unit" *AU*.

$$1\ AU = \frac{1.22\bar{\lambda}}{NA} \tag{23}$$

where $\bar{\lambda}$ is the wavelength of the illuminating laser light and *NA* the numerical aperture of the objective. *AU* is primarily used to normalize the pinhole diameter. *z*- and *x*-resolution is expressed by two terms; a wave-optical term and a geometric-optical term. At small pinhole diameter *PH* the geometric-optical effect on the pinhole can be neglected. As our measurements were conducted at *PH* = 1 *AU* the pinhole is not considered to be infinitely small. In this case, the optical slice thickness, resolutions in *z*- and *x*-direction are defined by following expressions: optical slice thickness:

$$\sqrt{\left(\frac{0.88\lambda_{\mathrm{em}}}{n-\sqrt{n^2-NA^2}}\right)^2+\left(\frac{\sqrt{2}n\cdot PH}{NA}\right)^2} \tag{24}$$

z-resolution:

$$\frac{0.88\lambda_{\mathrm{exc}}}{n-\sqrt{n^2-NA^2}} \tag{25}$$

x-resolution:

$$\frac{0.51\lambda_{\mathrm{em}}}{NA} \tag{26}$$

where $\lambda_{\mathrm{em,exc}}$ are the wavelength of the emitting and exciting light, respectively, *n* is the refractive index of immersion liquid, *NA* the numerical aperture of the objective and *PH* in μm. The calculated *z*- and *x*-resolution in the presented study is 2.15 μm and 0.46 μm, respectively.

The serial operation mode of a LSM leads to a limited temporal resolution of the measurement. Our measurements were

Table 3
Properties of the used fluids at 20 °C

Fluid	ρ (kg/m^3)	σ (mN m)	η (mPa s)
Ethanol	789.4	21.97	1.074
Water	998.3	74.54	1.025
20 wt% Glycerol in water	1050	70.2	1.76
40 wt% Glycerol in water	1103	68.2	3.72
60 wt% Glycerol in water	1155	66.9	10.8

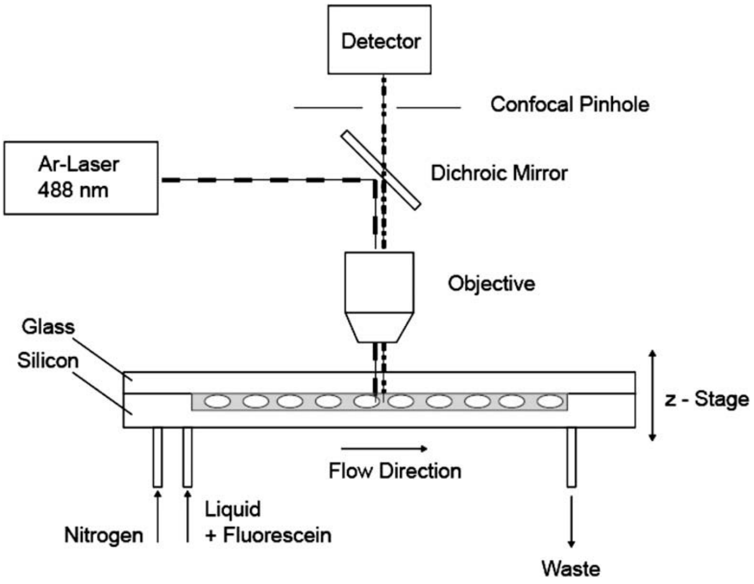

Fig. 3. Used experimental LSM-setup.

conducted with a pixel time of 0.81 μs, thus a frame of 1024 × 1024 *pixel*^{2} is recorded in 0.85 s. A stack of 200 optical slices was accomplished in 170 s.

Stationary Taylor flow in rectangular microfluidic channels is characterized by the alternating flow of gas bubbles and liquid slugs. The subsequent liquid slugs are connected to each other via liquid films at the channel wall and in the corners of the channel. The temporal resolution of the LSM is too low, that a sharp instantaneous 3D image of a channel section can be realized. To analyze time averaged films in Taylor flow, 1024 pictures in the direction of the channel length were averaged over a length of 420 μm. The regions of permanent liquid films are then indicated by higher intensity than the core region of the channel where gas and liquid passed by during the measurement. The measured liquid film thickness of the liquid film in our measurements is assumed to be constant and possible instationary effects are neglected. The data represents a time averaged thickness of the liquid at the wall and can also be interpreted as region with highest probability of liquid being present surrounding the gas bubble.

3.2.2. Image processing

Fluorescence microscopy is used to visualize the liquid phase distribution in the microfluidic channel. Fluorescein (peak emission = 520 nm) is added to the liquid phase and excited with a laser of 488 nm wavelength. A low pass filter provides only the emitted light to be detected by the photomultiplier.

During measurement the microreactor is placed on a precision stage connected via flexible tubing to gas and liquid feed described in Section 2. We used a 20× long working distance objective ($NA = 0.6$) with correction for different cover glass thicknesses. The correction was needed for a correct reproduction of the length scales in depth through the glass cover of the microfluidic channel. Optical slices in channel depth were recorded with a confocal laser scanning microscope (LSM 5 Pascal, Zeiss). The frame size was 1024 × 1024 *pixel*^{2} corresponding to a field of view of 420 × 420 μm^2. The optical slice thickness was 0.41 μm. Since only the films at the top of the microfluidic channel were observed, the stack size in *z*-direction was 75–100 μm. The pinhole diameter was set to a constant value of 112 μm, corresponding to 1 AU. The acquisition time for one pixel was 0.81 μs and two measurements were averaged per pixel for better statistics.

Fig. 4 shows the schematic operations of the data analysis. The acquired images are time averaged pictures of subsequently passing liquid slugs and gas bubbles. By averaging the images in flow direction, regions of permanent liquid coverage have a significant increased intensity compared to regions where both gas and liquid pass through during the acquisition time of a stack of pictures. Edges of the liquid regions and thresholds were detected using the software Matlab. The optical slices were acquired and stored as a stack pictures (Fig. 4(a)). When a *xy*-frame was recorded, 55% or more of the frame is covered by gas, hence has zero intensity. The stack then was sliced in *x*-direction, where each frame represented a slice in direction of the channel length (Fig. 4(b)). By averaging all 1024 *yz*-frames, a distinction between permanently wetted areas and areas of passing liquid and gas can be made via thresholding (Fig. 4(c)). The wall film at the channel top (δ_f) and in the film in the two corners (δ_c) were determined by a Matlab program (Fig. 4(d)). The robustness of the method was verified by threshold variation.

The channel top wall, the schematic bubble shape and the film width are indicated by the white lines. The channel walls could be indicated clearly by applying an automated threshold at the channel edges. Light scattering on the transition from the glass to the thin liquid film and from the liquid film to the gas phase was taken into account for the identification of the film thickness. The wall film thickness was defined by the length from the channel edge to the first minimum intensity. This region showed the highest intensity values and therefore the other parts of the wall film were assigned to light scattering. The corner film thickness was calculated by the diagonal distance between the channel corner and the transition from liquid to the gas phase.

The wall film width was analyzed from the intensity profile at the top channel wall and is indicated by the white lines in Fig. 4(d). Higher intensities represent liquid present at the wall. The two minima of the intensity distribution indicate the transition from the corner film to the wall film at the top channel wall. The distance between these points is defined as the film width *w*.

4. Results and discussion

4.1. Slug length

Analyzing the slug lengths over the complete channel length result in a constant slug length, except for ethanol. In contrast to water and glycerol, the evaporation of ethanol was observed with-

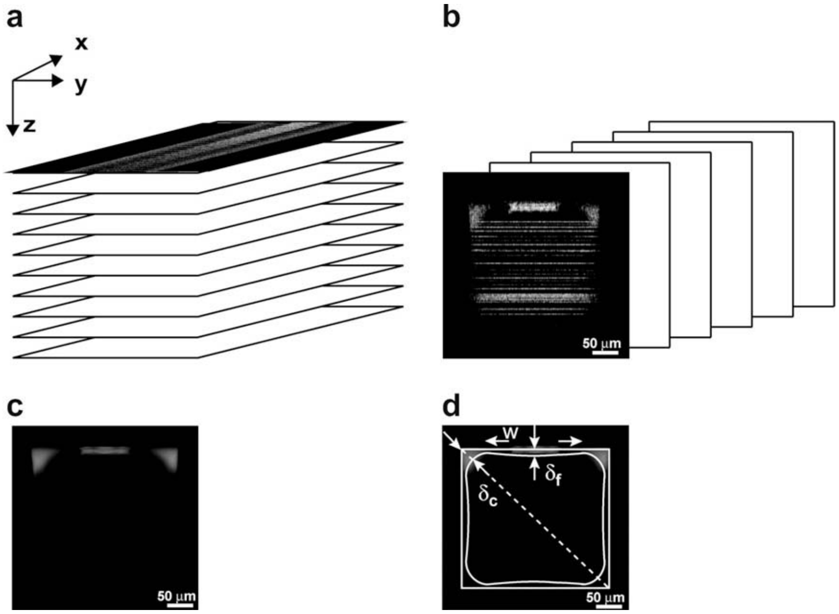

Fig. 4. Scheme of data analysis for the determination of the film thickness. (a) Optical slices in direction of the channel depth recorded with the LSM. (b) Reconstruction of *yz* slices. (c) Average image of all *yz* slices in channel length direction. (d) Average image of the channel cross section with a schematic outline of the channel wall and observed films. Film thicknesses at the channel top (δ_f) and in the corner (δ_c) were measured.

in the first 700 mm in the reactor. For comparison reasons, we use the slug length 105 mm behind the gas inlet for the following considerations. The measured slug lengths are summarized in Fig. 5. In general, the slug length increases with increasing superficial liquid velocity at a constant gas flow rate. At theoretical holdup values (see Eq. (17)) larger than 0.25 an increase in the viscosity will result in higher liquid slug lengths. Lower ϵ_L^*-values result in constant liquid slug lengths for increasing viscosity values. The slug lengths are not as stable as the gas bubble lengths: standard deviations are in the range of 10%, for high liquid rates at a given gas flow rate even higher.

4.2. Bubble length

The bubble length was analyzed over the complete channel length. Due to the pressure drop in the channel an elongation of the bubbles was observed. To verify the pressure drop as reason for this elongation, the pressure was measured at the liquid inlet and at the liquid outlet. Note, that due the capillary at the outlet the pressure at the liquid outlet is not the atmospherical one. Assuming ideal gas behavior and neglecting turns and manifolds as pressure resistance, we calculate the gas bubble length according to the measured pressure drop and the gas bubble length closed to the gas inlet:

$$p_1 \cdot V_1 = p_2 \cdot V_2 \Rightarrow p_1 \cdot l_{B,1} = p_2 \cdot l_{B,2} = p(L) \cdot l_B(L). \tag{27}$$

The subscripts 1 and 2 characterize an arbitrary position in the reactor. Assuming $\Delta p \backsim L_R$ leads to

$$p(L) = \frac{\Delta p_{tot} \cdot L_R}{L} \tag{28}$$

In Fig. 6 the measured gas bubble length l_B is plotted over the reactor length L_R for ethanol-nitrogen. It can be seen, that the gas bubble

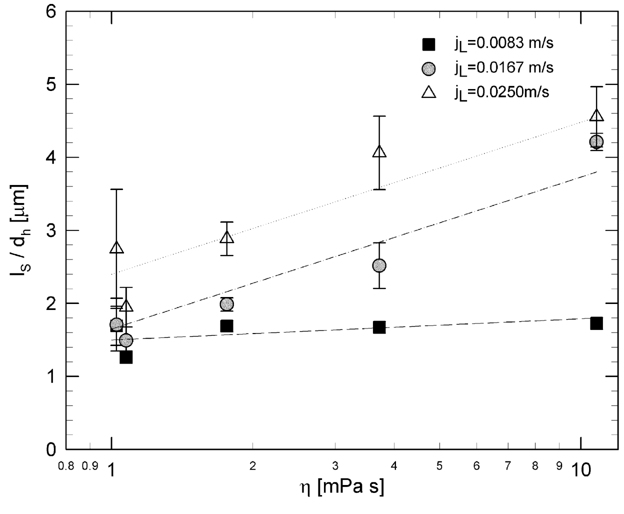

Fig. 5. Measured slug lengths 105 mm behind the gas inlet. Superficial gas velocity was in all cases j_L = 0.0416 m/s. Lines are best fit.

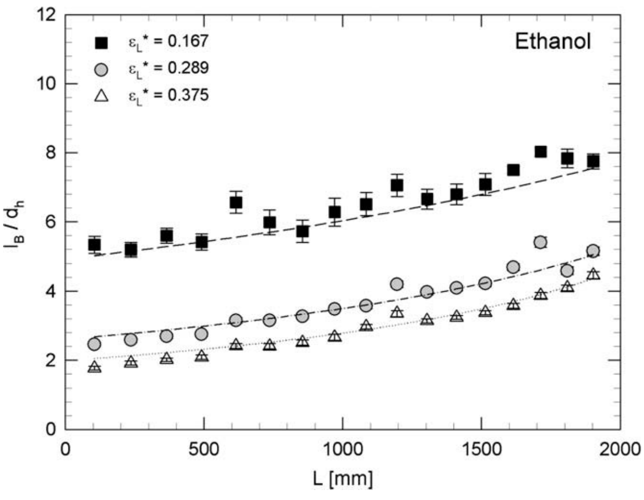

Fig. 6. Bubble length over the reactor for ethanol–nitrogen at constant j_G = 0.0416 m/s and varying j_L. Dotted lines represent the calculated values by Eq. (28).

length depends on the pressure and, for a constant superficial gas velocity of 0.042 m/s, on the superficial liquid velocity: an increase in the liquid flow rate results in a decrease of the gas bubble length. The gas bubble elongation is caused only due to the pressure drop, no coalescence was observed. The dotted lines with the calculated gas bubble length based on the measured pressure drop and Eq. (28) fit the measured bubble lengths with a correlation coefficient of 0.99. For the other fluid pairs the same trend was observed.

In Fig. 7(a) the dimensionless gas bubble length is plotted versus the viscosity at the gas inlet. Increase of the viscosity leads to decreasing bubble length. At low liquid flow ratio, the gas bubbles are longer compared to high liquid flow rates. The measured standard deviation of the gas bubble length is in all cases around 5%, only for water as liquid phase standard deviations in the range of 10% were observed. The bubble length variation is influenced by the geometrical situation at the gas inlet. Additionally a non-pulsating liquid pump and a constant gas flow rate are the basics for a stable flow. The bubble breakup procedure at the gas inlet is very sensitive to small changes in the flow rate, to changes in the surface tension (Marangoni effects) and to the geometry, including the wall roughness (Garstecki et al., 2006). As the geometry is kept constant for all experiments, the higher fluctuations for the gas bubble length for low-viscosity liquids indicates the sensitivity. In Fig. 7(b) the calculated bubble length for atmospheric pressure is plotted versus the viscosity. It is important to note that increasing viscosity leads to increase in gas bubble length at standard conditions.

4.3. Pressure drop

As described in Section 1.1, the pressure drop consists of pressure drop due to acceleration, due to gravity and due to surface tension. The acceleration forced pressure drop was for all measurements below 100 Pa (Eq. (2)). The pressure drop due to gravity (Eq. (3)) can be neglected due to the horizontal position of the microreactor. The pressure drop due to the surface tension (Eq. (4)) is in the same range than the pressure drop due to acceleration. Therefore the pressure drop in our experiments was assumed to consist only of the frictional pressure drop (Eq. (6)).

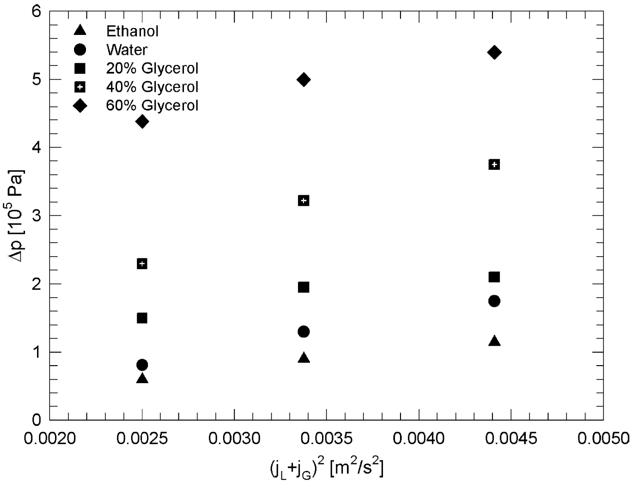

Fig. 8. Measured pressure drop as function of square of the total superficial velocity.

The overall pressure drop was measured between the liquid inlet and the liquid outlet. The results are shown in Fig. 8, indicating that the pressure drop depends on the sum of the superficial velocities and on the fluid properties. Increasing the velocity leads to an enhanced pressure drop. The increase is linear to the square of the velocity. Less viscous fluids give smaller pressure drop values than fluids with a higher viscosity. A decrease of the pressure drop is obtained by increasing the surface tension. Note, that these conclusions are only valid if all other parameters are kept constant. A change in the surface tension and/or in the viscosity varies the slug length, as shown in Section 4.1. Due to the recirculation movement shorter liquid slugs lead to enhanced pressure drop per unit length. In Fig. 9(a) the measured pressure drop values are compared with literature models (Table 1): the homogenous model, where the friction factor is calculated by $f = 16/Re$ and the models by Bretherton (1961) and Kreutzer et al. (2005b), which include correction factors for the pressure drop due to the recirculation in the liquid slug. Obviously the one-phase model underpredicts the pressure, which is consistent with literature. The model of Bretherton (1961) describes the experimental results better than the model of Kreutzer et al. (2005b). It should be noted, that the factor $\tau = 0.17$ in the model of Kreutzer et al. (2005b) was found empirically for a round capillary with $d_h = 2.3$ mm. We fitted this factor by the least square method and obtained the best result for $\tau = 0.28$. The underprediction of the model by Kreutzer et al. (2005b) has two reasons: first, we use a rectangular channel with $d_h = 0.2$ mm, whereas (Kreutzer et al., 2005b) used a circular capillary with a diameter of $d_h = 2$ mm. The difference of the diameter

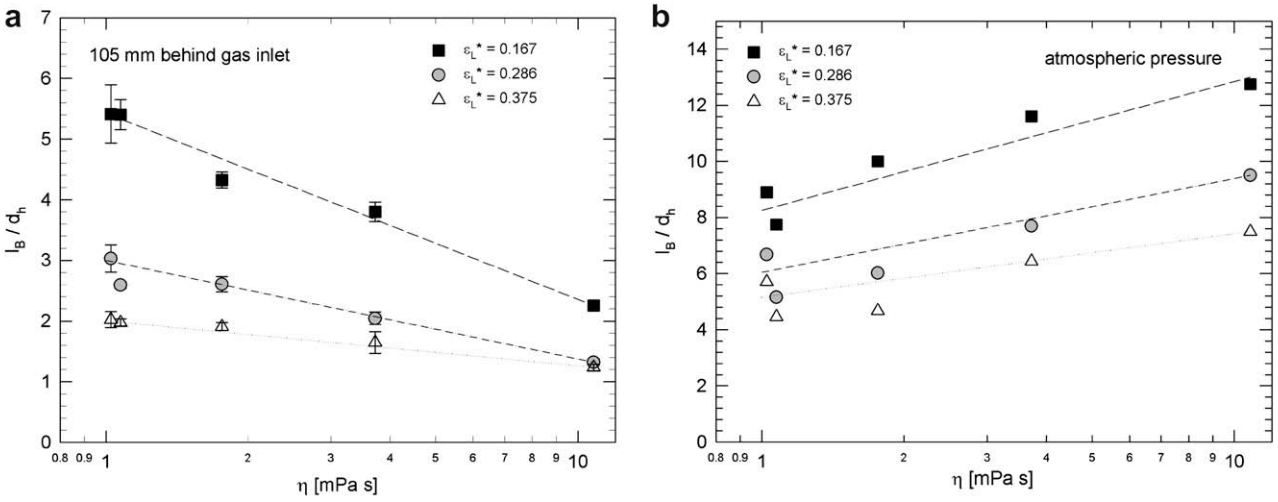

Fig. 7. Gas bubble length versus viscosity. Lines represent best fit. (a) Bubble lengths 105 mm behind the gas inlet. (b) Corrected bubble lengths for atmospheric pressure.

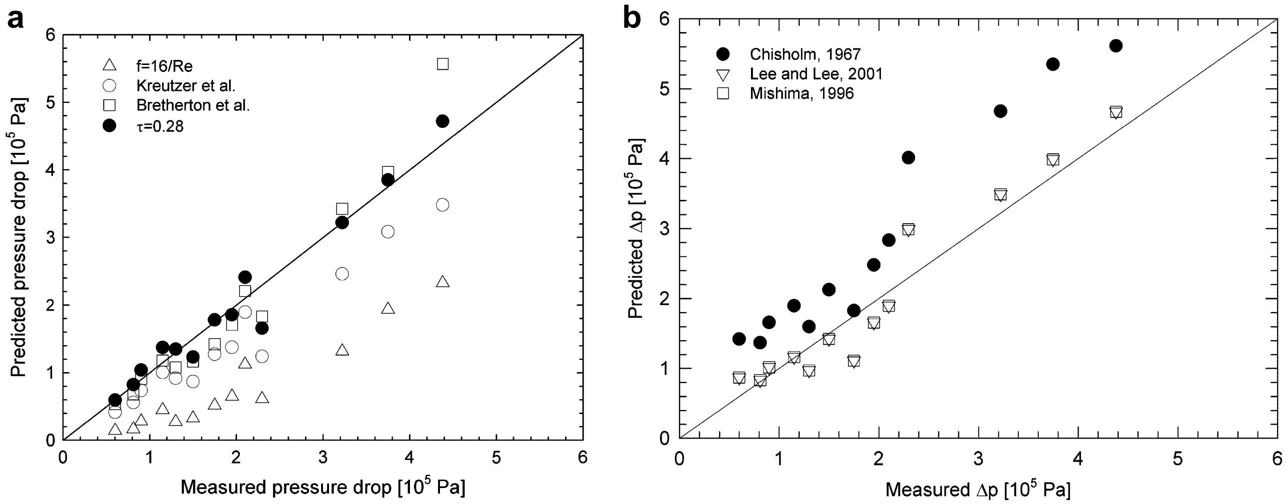

Fig. 9. Comparison of the measured pressure drop with literature models based on the one phase pressure drop (a) and the model proposed by Lockhart-Martinelli (b).

by one magnitude should have no influence, as $Bo = \rho d_h^2 g/\sigma$ is in both cases below 3. To our opinion, the non-constant film surrounding a bubble in a rectangular microchannel and the wall roughness, which is more important in microstructures, leads to an elevated pressure drop. The models based on the Lockhart–Martinelli theory (Eq. (10)) are depicted in Fig. 9(b). Good agreement for the models based on microchannels is observed, whereas the model developed for circular pipes in the macro scale overpredicts our measurements.

4.4. Phase distribution

As can be seen in Fig. 10, the liquid holdup at atmospheric pressure corresponds reasonable to the volumetric flow rate. The liquid holdup changes significantly by passing the reactor due to the pressure drop.

Additional, the ratio and the sum of the gas bubble lengths and the liquid slug lengths can be used to characterize the flow. We consider the ratio of the gas bubble lengths to the liquid slug lengths close to the reactor inlet as it is illustrated in Fig. 11. These results give an information about the bubble breakup at the gas inlet. Due to different pressure drop values, the pressure at the inlet changes for different liquids and velocities. A clear tendency can be seen: the bubble-to-slug-length ratio depends strongly on the viscosity and the velocity rate, whereas increasing the viscosity leads to a decreasing bubble-to-slug-length ratio.

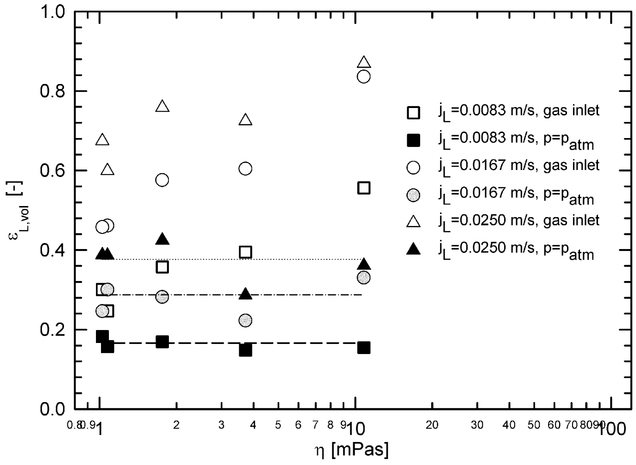

Fig. 10. Liquid holdup versus the viscosity. The superficial gas velocity was in all experiments 0.0416 m/s.

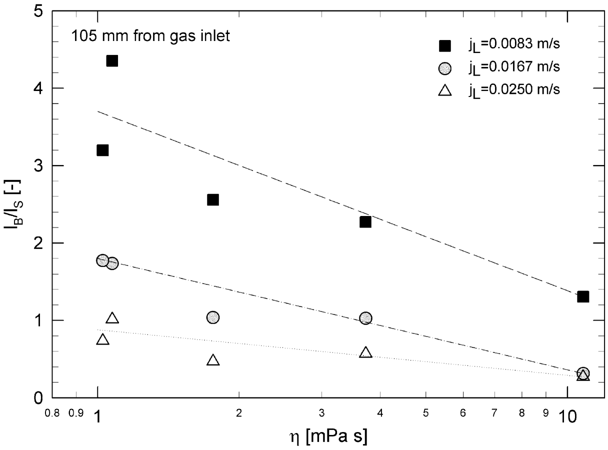

Fig. 11. Bubble-to-slug ratio 105 mm behind the gas inlet for different velocity rates. The superficial gas velocity was in all experiments 0.0416 m/s. Lines are best fit.

4.5. Velocities

Bubble velocities are plotted in Fig. 12 versus the sum of the superficial inlet velocities at inlet conditions. Obviously, the measured velocity gives higher values than the corresponding superficial inlet velocity. An exception must be made for the flow of 60% glycerol for superficial liquid velocities of $j_L = 0.0167$ m/s and $j_L = 0.025$ m/s. As mentioned before, the flow properties for these two experiments were different to experiments at lower viscosities. The higher measured bubble velocities compared to the superficial velocities indicate, that the effective channel area available for the gas phase is smaller than the total channel area. This means, that a liquid film with a lower velocity covers some part of the channel. The result indicates that the bubbles move faster than the liquid slugs.

4.6. Film thickness

The data from confocal microscopy are used to analyze quantitatively film thickness and film width.

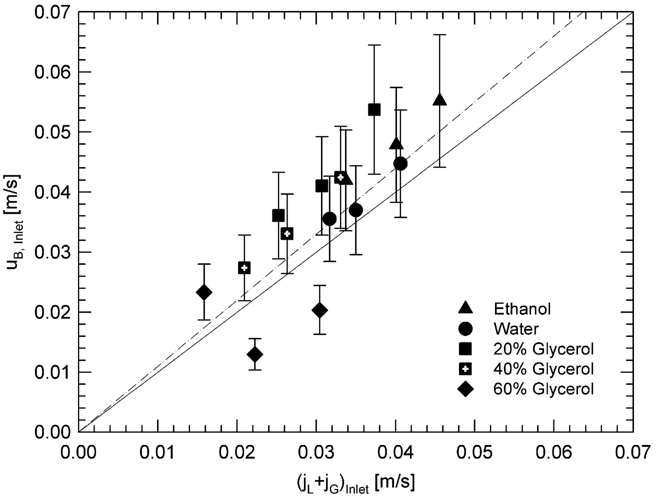

Fig. 12. Measured bubble velocity versus the superficial inlet velocity. The straight line indicates $u_B = j_G + j_L$, the dotted line $u_B = 1.1\ (j_G + j_L)$.

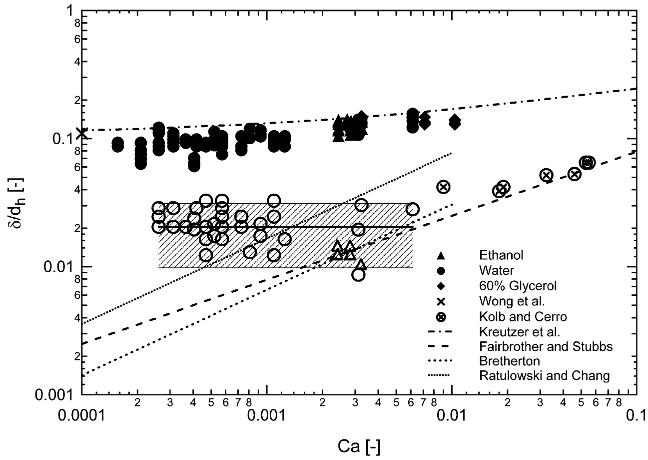

Fig. 13. Measured film thicknesses for different fluids. Filled symbols represent the film thickness in the corner and open symbols the wall film thickness, respectively.

Results of film thicknesses are plotted, together with correlations from literature, in Fig. 13. First, we consider the situation at the corner. The correlation done by Kreutzer et al. (2005a) slightly overpredicts the film thickness of the experimental data. This correlation was used for *Ca* values ranging from 2×10^{-4} to 10. The general decreasing tendency with decreasing *Ca* is the same for the measured values and the model. The difference is more pronounced at low *Ca*, where shorter bubbles in the segmented gas liquid flow occur. At higher *Ca* the gas bubbles elongate and the measurements are better comparable to literature, where mostly semi-infinite gas bubbles at higher *Ca* were measured. For small *Ca* ($Ca < 0.001$) the corner film thickness is nearly independent from the *Ca*. The ratio of the film thickness in the corner to the hydraulic channel diameter remains constant at around 0.1.

For the film thickness at the wall, the model by Bretherton (1961) (Eq. (20)) proposes a dependency of $Ca^{2/3}$, also for small *Ca*. The measurements done by Kolb and Cerro (1991) for a semi-finite gas bubble lead to the assumption, that for $Ca < 0.01$ no significant change of the film thickness for further reducing *Ca* occurs. Using a smaller channel, our measurements confirm this trend. For $Ca < 0.01$, the ratio of the film thickness at the wall to the hydraulic channel diameter is constant at a value around 0.02. Due to the limited optical resolution, the uncertainty of the measurements in this range is relative high. The measured film thickness is around $\delta_f = 4$ μm, and the resolution in the *z*-direction is ±2.15 μm. Therefore the mean value of the measurements is indicated in Fig. 13 with the according expected measurement error. It is seen that the majority of the measurements are within this interval. The model by Fairbrother and Stubbs (1935) (Eq. (18)), which gives reasonable agreement with experimental results for $Ca > 0.1$ cannot be adapted to the measurements at $Ca < 0.01$. At low *Ca* none of the existing correlations describe the experimental data.

By other authors, there was always a significant deviation of experimental results of wall film thickness compared to Bretherton's theory. Thicknesses larger than theory were measured at very low *Ca*. The larger values were contributed either to the surface roughness (Chen, 1986) or to small amounts of adsorbed surface-active contaminants on the gas–liquid interface (Ratulowski and Chang, 1990). In regions of high surfactant concentrations (bubble front) the interface becomes more rigid. At low surfactant concentration (film) the surface tension is larger and induces more liquid to flow into the film. This leads to an increased wall film thickness. The latter theory was developed for long gas bubbles ($l_B > 20d_h$), therefore it is difficult to adapt the results to Taylor flow with bubble length in the order of a few channel diameters. In Fig. 13 the correction of Brethertons theory for Maragoni effects is shown (Ratulowski and Chang). Additionally the theory by Bretherton is applicable for circular capillaries. In our case of a square microchannel, the wall film thickness is developing on a flat area. In case of low *Ca*, the situation is reduced to a static wetting problem assuming zero velocity in the film. The film thickness then is defined only by the surface tension of the fluid and the wall material. As inertial effects are negligible, a constant film thickness is obtained. This corresponds to the theory of the corner wall thickness, where an asymptotic value for the thickness at $Ca \to 0$ is obtained (Wong et al., 1995).

4.7. Film width

Fig. 14 shows that the film width is decreasing with increasing *Ca*. This corresponds to the slightly increasing corner film thickness. With increasing corner liquid volume the gas bubble becomes more symmetric and the film width decreases (compare Fig. 1). Former studies reported an axial symmetric gas bubble (body) at higher values of $Ca \approx 0.1$ (Kolb and Cerro, 1991). Our measurements were done at lower *Ca* numbers, that this transition cannot be observed.

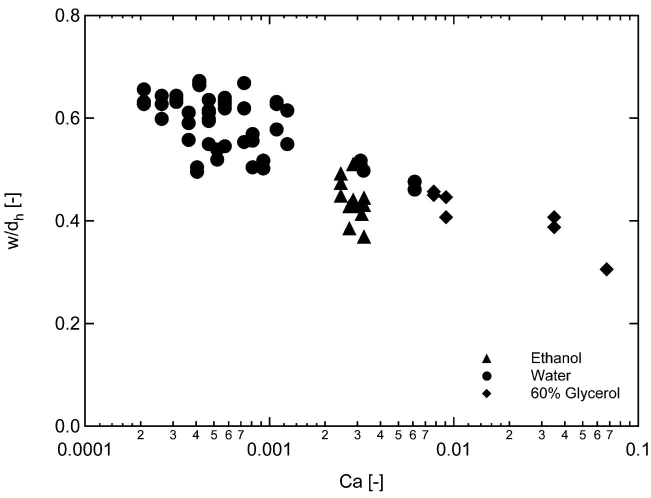

Fig. 14. Measured wall film width at different *Ca*.

4.8. Film area

The total film area in a channel cross section was calculated assuming a tangential transition from the corner film to the wall and a rectangular shape of the wall film which is calculated with the measured thickness and width. The corner film area can be expressed as $A_c = 4r_c^2(1 - \pi/4)$. r_c defines the radius of the gas bubble in the corner, which can be calculated using geometrical constraints reported in Kolb and Cerro (1991). The wall film area is defined as $A_f = 4\ \delta_f w$. The relationship between film area, the bubble velocity (u_B) and the liquid slug velocity (u_S) can be investigated from the overall mass balance between a cross section where gas and liquid is present and a cross section through the liquid slug. At steady state and incompressible conditions, assuming zero velocity in the liquid film for horizontal flow, the mass balance leads to the relation

$$A_B u_B = A_{Channel} u_S \tag{29}$$

where A_B is the area occupied by the gas bubble and $A_{Channel}$ the cross section of the channel. This leads to

$$1 + \frac{A_c + A_f}{A_{Channel}} = \frac{u_B}{u_S}. \tag{30}$$

Eq. (30) shows that the bubble velocity is always faster than the liquid slug velocity, since the corners of the microchannel are always wetted by liquid and therefore the total film area ($A_f + A_c$) does not vanish.

The film area is difficult to obtain, since the transition area from the wall film to the corner film is hard to resolve. An approximation of the area lead to a ratio of $(A_f + A_c)/A_{Channel}$ of about 10% for a water/nitrogen mixture at $Ca = 0.003$. With Eq. (30) a velocity of the bubble in the same range is also confirmed in Fig. 12. The corners contribute at the measured Ca number with about 70% to the total film area. Theoretical limits for the liquid covered area are known from literature (Kreutzer et al., 2005a). At $Ca \to \infty$ the total film area covers 61.5% of the channel area. Assuming only corner films at $Ca \to 0$ and a maximal bubble diameter in the diagonal direction of 1.2 d_h the minimal total film area is 5.7%.

5. Conclusion

In this article, we characterized Taylor flow in a 2 m long rectangular microchannel by optical methods and pressure drop measurements. The microchannel was designed for minimal disturbance of the sensitive flow by the inlet and outlet. A detailed analysis of the liquid slug length, the gas bubble length, the pressure drop, the liquid holdup, the bubble velocity and the liquid film is provided.

The liquid slug length increases with increasing viscosity. This effect is more pronounced for higher liquid velocities at constant gas velocity. The slug length varies between $O(d_h)$ for low viscosity and velocity and $O(4d_h)$ for high viscosity and velocity.

At constant pressure, the bubble length increases with increasing viscosity where higher liquid velocities lead to decreasing gas bubble lengths. The pressure drop was correlated with different models. Best agreement was obtained with the correlation of Bretherton (1961). An adapted correlation for the friction factor based on the model of Kreutzer et al. (2005a) was presented. The liquid holdup varies significantly along the channel length due to the pressure drop.

A long channel is required for chemical reactions with longer residence times as well as for neglecting the effects of manifolds as the inlet and the outlet. A tradeoff between the pressure drop and the reactor length is mandatory.

The bubble velocity was found to be about 10% higher than the sum of the corresponding superficial velocities. For small Ca, only small dependencies of the dimensionless film thickness in the corner as well as at the wall were observed. In this Ca range, a wall film thickness of constant size is due to the dominating surface tension and therefore mainly depending on the wetting properties. The wall film width decreases with increasing Ca according to a more symmetrical gas bubble shape. The area covered by the film consists of 10% of the total cross section, which is identical to the increased gas bubble velocity compared to the total superficial velocities.

These results allow in a further mass transfer analysis the determination of (i) degree of axial dispersion between neighboring liquid slugs through the film (ii) gas–liquid-interfacial area for gas–liquid mass transfer (iii) mass transfer through the liquid film to the wall in case of catalytic reaction. Further investigations have to focus on the velocity profile in the liquid film by μ-Particle Image Velocimetry.

Acknowledgements

This work was financially supported by the ETH Research Grant TH-32/05-2 and the Emil Barell foundation. We thank the group of Prof. Boulouchos at ETH for the high speed camera equipment.

References

Aussillous, P., Quere, D., 2000. Quick deposition of a fluid on the wall of a tube. Phys. Fluids 12, 2367–2371.

Bretherton, F., 1961. The motion of long bubbles in tubes. J. Fluid Mech. 10, 166–188.

Chen, J.D., 1986. Measuring the film thickness surrounding a bubble inside a capillary. J. Colloid Interface Sci. 109, 341–349.

Chisholm, D., 1967. A theoretical basis for the Lockhart–Martinelli correlation for two-phase flow. Int. J. Heat Mass Transfer 10, 1767–1778.

de Mas, N., Günther, A., Schmidt, M.A., Jensen, K.F., 2003. Microfabricated multiphase reactors for the selective direct fluorination of aromatics. Ind. Eng. Chem. Res., 698–710.

Fairbrother, F., Stubbs, A.E., 1935. Studies in electro-endosmosis part vi the "bubble-tube" method of measurement. J. Chem. Soc. 1, 527–529.

Fletcher, P.D.I., Haswell, S.J., Zhang, X.L., 2003. Monitoring of chemical reactions within microreactors using an inverted Raman microscopic spectrometer. Electrophoresis 24, 3239–3245.

Friedel, L., 1978. Druckabfall bei der strmung von gas/dampf-flssigkeitsgemischen in rohren. Chemie Ingenieur Technik 50, 167–180.

Garstecki, P., Fuerstman, M., Stone, H., Whitesides, G., 2006. Formation of droplets and bubbles in a microfluidic T-junction scaling and mechanism of break-up. Lab Chip 6, 437–446.

Günther, A., Thalmann, M., Jhunjhunwala, M., Schmidt, M.A., Jensen, K.F., 2005. Micromixing of miscible liquids in segmented gas–liquid flow. Langmuir 21, 1547–1555.

Hazel, A.L., Heil, M., 2002. The steady propagation of a semi-infinite bubble into a tube of elliptical or rectangular cross-section. J. Fluid Mech. 470, 91–114.

Irandoust, S., Andersson, B., 1989. Liquid film in taylor flow through a capillary. Ind. Eng. Chem. Res. 28, 1684–1688.

Jensen, K.F., 2001. Microreaction engineering – is small better? Chem. Eng. Sci. 56, 293–303.

Khan, S.A., Günther, A., Schmidt, M.A., Jensen, K.F., 2004. Microfluidic synthesis of colloidal silica. Langmuir 20, 2004.

Kinoshita, H., Kaneda, S., Fujii, T., Oshima, M., 2007. Threedimensional measurement and visualization of internal flow of a moving droplet using confocal micro-piv. Lab Chip 7, 338–346.

Kolb, W.B., Cerro, R.L., 1991. Coating the inside of a capillary of square cross section. Chem. Eng. Sci. 46, 2181–2195.

Kreutzer, M., Günther, A., Yen, B., Jensen, K.F., 2006. On-chip measurement in segmented flow through microchannels. In: AIChE Annual Meeting. San Francisco, CA, p. 150.

Kreutzer, M., Kapteijn, F., Moulijn, J., Heiszwolf, J., 2005a. Multiphase monolith reactors: chemical reaction engineering of segmented flow in microchannels. Chem. Eng. Sci. 60, 5895–5916.

Kreutzer, M., Kapteijn, F., Moulijn, J., Kleijn, C., Heiszwolf, J., 2005b. Inertial and interfacial effects on pressure drop of taylor flow in capillaries. AIChE J. 51, 2428–2440.

Lee, J.H., Lee, Y.S., 2001. Pressure drop correlations for two-phase flow within horizontal rectangular channels with small heights. Int. J. Multiphase Flow 27, 783–796.

Lockhart, R., Martinelli, R., 1949. Proposed correlation of data for isothermal two-phase, two-component flow in pipes. Chem. Eng. Prog. 45, 39–48.

Marchessault, R.N., Mason, S.G., 1960. Flow of entrapped bubbles through a capillary. Ind. Eng. Chem. 52, 79–84.

Mishima, K.H.T., 1996. Some characteristics of air–water two-phase flow in small diameter vertical tubes. Int. J. Multiphase Flow 22, 703–712.

Park, H., Qiu, X., Rhoades, E., Korlach, J., Kwok, L., Zipfel, W., Webb, W., Pollack, L., 2006. Achieving uniform mixing in a microfluidic device: hydrodynamic focusing prior to mixing. Anal. Chem. 78, 4465–4473.

Ratulowski, J., Chang, H.C., 1990. Marangoni effects of trace impurities on the motion of long gas-bubbles in capillaries. J. Fluid Mech. 210, 303–328.

Stroock, A., Dertinger, S., Ajdari, A., Mezic, I., Stone, H., Whitesides, G., 2002. Chaotic mixer for microchannels. Science 295, 647–651.

Taha, T., Cui, Z.F., 2006. CFD modelling of slug flow inside square capillaries. Chem. Eng. Sci. 61, 665–675.

Taylor, G., 1961. Deposition of a viscous fluid on the wall of a tube. J. Fluid Mech. 10, 161–165.

Thulasidas, T.C., Abraham, M.A., Cerro, R.L., 1995. Bubble-train flow in capillaries of circular and square cross-section. Chem. Eng. Sci. 50, 183–199.

Trachsel, F., Günther, A., Khan, S.A., Jensen, K.F., 2005. Measurement of residence time distribution in microfluidic systems. Chem. Eng. Sci. 60, 5729–5737.

Waelchli, S., Rudolf von Rohr, P., 2006. Two-phase flow characteristics in gas–liquid microreactors. Int. J. Multiphase Flow 32, 791–806.

Wong, H., Radke, C.J., Morris, S., 1995. The motion of long bubbles in polygonal capillaries. 1. Thin-films. J. Fluid Mech. 292, 71–94.